Ionizing Radiation Effects Spectroscopy for Analysis of Single Event Transients

T. D. Loveless, *Senior Member, IEEE,* B. Patel, *Student Member, IEEE,* D. R. Reising, *Senior Member, IEEE,* R. Roca, M.Allen, L. W. Massengill, *Fellow, IEEE,* and D. McMorrow, *Fellow, IEEE*

***Abstract*—Ionizing radiation effects spectroscopy (IRES) for characterization of single-event transients (SET) in space-deployed electronics is demonstrated. IRES enhances time-frequency spectroscopy techniques with statistical analysis, allowing for the capture of subtle changes in circuit dynamics. This is illustrated through the use of experimental data captured from two-photon absorption (TPA) laser experiments on a phase-locked loop (PLL) designed and fabricated in a 130 nm CMOS technology, and further explained through the use of behavioral modeling of the PLL. The technique leverages the computational benefits of discrete windowed analysis, requiring as little as 0.2% of the data samples required in high-resolution discrete Fourier transform analysis while providing a statistical method for accurately estimating the SET characteristics.**

***Index Terms*—Ionizing Radiation Effects Spectroscopy, Phase Locked Loops, Radiation Effects, Single Event Effects, Single Event Transients, Spectroscopy, Time Frequency Analysis, Two Photon Absorption.**

I. Introduction

THE mitigation of transient radiation effects is generally accomplished through the increase of capacitance, device size, and current drive in order to increase the critical charge required to generate single-event transients (SETs). This type of circuit hardening occurs at the cost of significant area, power, and bandwidth penalties [1], [2], and minimizing these design penalties requires knowledge of the primary radiation vulnerabilities as well as the potential responses of the circuit or system. *A priori* knowledge is particularly challenging for complex analog and mixed-signal (hybrid analog and digital) electronics with large state spaces and many potential signal paths for SETs. Moreover, there exists no standard metric for SETs in analog and mixed-signal systems (AMS), as the effect of a single event (SE) is dependent on the circuit topology, type of circuit, and the operating mode [3]. This uncertainty can result in over design and application-specific mitigation solutions.

One standard method for analyzing the severity of SETs is through measurement of the magnitude of the erroneous voltage or current and the time duration (pulse width) of the events [1]–[3]. The resulting magnitude versus pulse width scatter plots allow for a coarse classification of events and are useful for employing filter-based mitigation schemes between circuits [1], [3]. However, it is difficult to measure these characteristics *in situ*; it is often the case that devices are biased in static modes for ease of measurement, rather than under the intended operational conditions.

This work uses experimental measurements and simulations on a phase-locked loop (PLL) circuit fabricated in a 130 nm CMOS process [4], [5] to demonstrate transient analysis under dynamic operating conditions and radiation exposure. However, the techniques presented herein apply to any circuit or system through the analysis of the output waveform behavior. Data presented in Section II were captured from two-photon absorption (TPA) laser experiments [5]–[9] on the PLL designed and fabricated in a 130 nm CMOS technology. Then, in Section III, spectrographic techniques are discussed for general use in AMS and radio frequency (RF) circuits to assist in the identification of transient anomalies *in situ* without the need for internal node interrogation. Spectrographic techniques, such as the Short-Time Fast-Fourier Transform (STFT) [10] for viewing the frequency and phase content of a signal versus time are augmented with ionizing radiation effects spectroscopy (IRES) in Section IV for quantifying the statistical behavior of the waveforms, which allows for a low-overhead mechanism for isolating the erroneous signatures embedded within a signal.

These data illustrate that SET waveforms contain spectral characteristics that are unique to the strike origin, circuit state, and operating conditions, quantifiable through statistical information. Simulations conducted using a behavioral model of the PLL further emphasize the utility of the technique for identifying subtle changes in signals associated with circuit anomalies and instability. Further, these results indicate that SET spectral content is unique and predictable based on the ionizing particle interactions and circuit responses.

Manuscript received July 7, 2019. Revised manuscript received Oct. 17, 2019.

T. D. Loveless, B. Patel, D. R. Reising, R. Roca, and M. Allen are with the Electrical Engineering Department, University of Tennessee at Chattanooga, 615 McCallie Ave., Dept. 2342, Chattanooga, TN, 37403, USA; (phone: 423-425-2353; fax: 423-425-5229; e-mail: daniel-loveless@utc.edu).

L. W. Massengill is with the Department of Electrical Engineering and Computer Science, Vanderbilt University, VU Station B #351824, 2301 Vanderbilt Place, Nashville, TN 37235-1679, USA; (e-mail: lloyd.massengill@vanderbilt.edu).

D. McMorrow is with the Naval Research Laboratory, Washington, D.C., USA; (e-mail: dale.mcmorrow@nrl.navy.mil).

This work was supported in part by the Department of the Navy, Office of Naval Research under ONR award number N00164-19-1-1004, the Department of Defense ASSURE program in partnership with the National Science Foundation (NSF) Research Experience for Undergraduate (REU) program under award number 1757777, the Tennessee Higher Education Commission (THEC) through the Center of Excellence in Applied Computational Science and Engineering (CEACSE) Program at the University of Tennessee at Chattanooga, and the Defense Threat Reduction Agency (DTRA) under contract HDTRA1-13-C-0063.

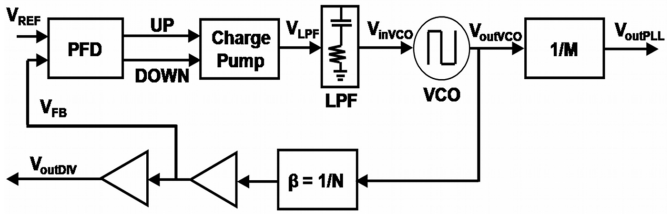

Fig. 1. Block diagram of the 130 nm CMOS PLL used to demonstrate transient spectrographic analysis techniques. The PLL consists of the phase-frequency detector (PFD), charge pump (CP), low-pass filter (LPF), voltage-controlled oscillator (VCO), and frequency divider (β). The PLL was designed with a center frequency of approximately 200 MHz (after [11]).

II. Device Under Test: The Phase-Locked Loop

A. PLL Electrical Characteristics

The block diagram of the charge pump (CP) PLL used to demonstrate the transient spectrographic analysis techniques in this work is shown in Fig. 1 [11]. While previous works have shown that the CP topology has an inherent vulnerability to SETs due to the high impedance output of the CP [2], [5], [11], [12], CP topologies are often used because of the high linearity and power supply noise rejection. Thus, the circuit is commonly found in integrated circuit (IC) clock generators and serves as a widely applicable demonstration vehicle for the spectrographic transient analysis techniques.

The CP PLL consists of the phase-frequency detector (PFD), charge pump (CP), low-pass filter (LPF), voltage-controlled oscillator (VCO), and frequency dividers. The dividers were set to unity for all experiments and simulations presented in this work. The PFD converts the difference in phase and frequency between the input reference signal (V_{REF}) and the PLL's output (V_{outPLL}) into electrical current through the CP. The activation of the CP to source/sink charge to/from the LPF capacitor C_{LPF} adjusts the voltage, V_{inVCO}, applied to the input of the VCO, thus modifying the output frequency of the VCO [4], [5].

The PLL was fabricated using a 130 nm CMOS technology available through the MOSIS foundry. The VCO has a center frequency (frequency at which $V_{inVCO} = V_{dd}/2$) and a maximum frequency of approximately 200 MHz and 530 MHz, respectively. The locking range of the PLL is between approximately 40 MHz and 350 MHz, over which the VCO is approximately linear with a gain of 7.75 GHz/V.

B. Experimental Setup

SETs were injected into the PLL circuit using laser-induced carrier generation based on TPA using high peak power femtosecond pulses at sub-bandgap optical wavelengths [6]–[9]. The device under test (DUT) was mounted on a motorized xyz translation platform with 0.1 μm resolution. In TPA, optical pulses are focused through the backside of the wafer onto the front surface of the DUT with a 100x microscope objective, resulting in a near-Gaussian beam profile with an approximate diameter of 1.6 μm at focus [9]. Because the carrier deposition varies as the square of the irradiance (I^2), this corresponds to a Gaussian carrier density distribution with an approximate diameter of 1.1 μm (full-width-at-half-maximum) [9]. This

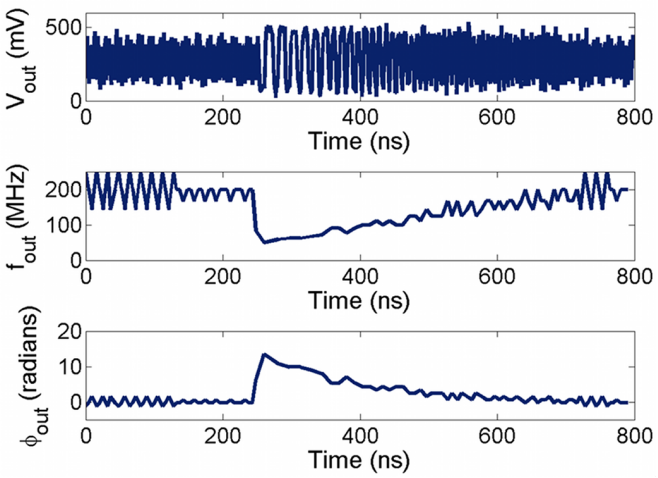

Fig. 2. Example of an output transient following a laser perturbation in the CP sub-circuit of the 130 nm PLL. The PLL was operating at 200 MHz prior to the laser strike. Following the laser strike, the output frequency was reduced to approximately 50 MHz, thus increasing the output phase displacement to approximately 15 radians. The recovery time of the PLL was over 200 ns [5].

work presents data from a single incident laser energy for various operating frequencies within the PLL's linear operating region. A single incident energy was chosen to ensure repeatability in the measurement, and to examine several aspects of the spectrographic analysis techniques discussed in the proceeding sections under control of constant energy transfer. Reference [5] reports transient data for various energy levels. All experiments were performed at room temperature with the nominal power supply voltage of 1.2 V.

In order to characterize output transients following laser strikes within the PLL, a Tektronix-TDS5104 oscilloscope was used to capture output waveforms at the sample rate of 625 MS/s. The oscilloscope was set to trigger on the rising edge of the pulsed laser sync pulse, and the FastFrame feature was utilized to capture ten transients per injection location. The experiment was performed by rasterizing the TPA laser through the CP sub-circuit at a step size of 0.2 μm. Figure 2 shows an example SET following a laser perturbation at the CP output node. Following the laser strike, the output frequency (f_{out}) was reduced to approximately 50 MHz, increasing the phase displacement (ϕ_{out}) to approximately 15 radians. The recovery time of the PLL was over 200 ns, corresponding to the PLL's initial lock time, indicating near-complete depletion of the charge stored on C_{LPF}.

Figure 3 illustrates a two-dimensional (2D) spatial map of the sensitive regions in the CP sub-circuit. Each pixel in the figure represents the average maximum phase displacement (instantaneous cycle-to-cycle phase error) for ten SETs generated at each x-y location [5]. The mapping of the output phase displacement versus x-y location was fused to a layout image of the CP sub-circuit. The dashed square represents the area interrogated by the TPA laser. Due to slight microscopic misalignment in the die and the measurement platform, the laser was traversed over the die slightly askew. The image illustrates that the output of the CP circuit, in particular the NMOS switches and current sources, contains

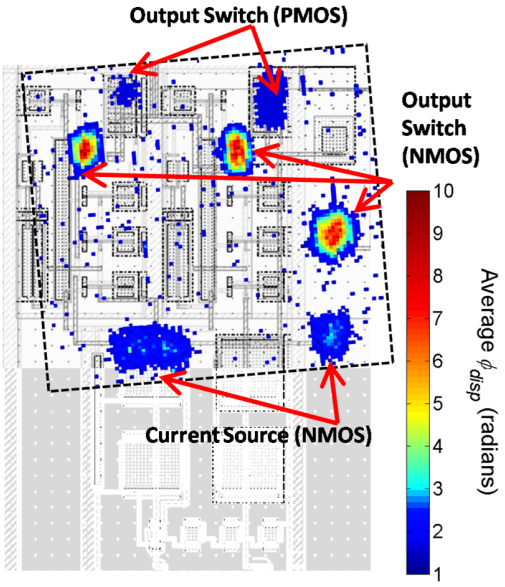

Fig. 3. A two-dimensional (2D) spatial map of the regions in the CP sub-circuit sensitive to SETs. The experiment was performed using laser TPA at a step size of 0.2 μm. Each pixel represents the average maximum phase displacement (instantaneous cycle-to-cycle phase error) for ten SETs generated at each x-y location. The image illustrates that the output of the CP circuit, in particular the NMOS switches and current sources contain the most sensitive junctions due to their ability to deplete the charge stored in C_{LPF} (after [5]).

the most sensitive junctions due to their ability to deplete the charge stored in C_{LPF}. The following sections employ various spectrographic analysis techniques for the identification and quantification of these transients. Short-time windowed spectroscopy techniques, in particular, the statistics-based method presented herein, allows for a detailed examination of transient phenomena with low computational overhead. The techniques are especially useful when analyzing noisy data.

III. Spectrographic Analysis

Spectroscopy has been employed in reliability applications for the extraction of the time-dependence associated with specific physical degradation phenomena [13]. In general, time-dependent spectroscopy involves the measurement of timing information associated with a defect or anomalous behavior, and the development of a statistical profile of such data. This work employs time-frequency spectral analysis and develops a methodology for quantifying the statistical parameters associated with SET behavior. This section delivers an overview of time-frequency spectrographic analysis. Section III.A discusses time-frequency Fourier analysis, overviewing the various tradeoffs associated with time and frequency domains. Then, in Section III.B, IRES is presented as a method to augment time-frequency analysis to isolate erroneous transient behavior embedded within dynamic waveforms.

A. Time-Frequency Analysis

A discrete sampling of signal $v_{out}(t)$ can be decomposed into its constituent frequencies through the Discrete Fourier Transform (DFT) [10] according to (1)

$$V(f_n) = \sum_{n=0}^{N-1} v_n e^{-\frac{j2\pi n}{N}} \quad (1)$$

where $v_n = v[n]$ is the N-point sampled sequence of signal $v_{out}(t)$ for $n = 0, 1, ..., N-1$. It follows that the power spectral density (PSD), S_v, can be determined through (2). PSD deconstructs the total signal power into a sequence of values representing the power for each frequency component (in units of dB/Hz) contained in the signal [14]. Thus, the integral of the PSD is the total signal power.

$$S_v(f_n) = \frac{1}{N}|V(f_n)|^2 \quad (2)$$

One-dimensional (1D) spectral analysis in either time or frequency domains is useful for steady-state signals. However, 1D spectral analysis has limited use for short-time transient effects. 2D joint time-frequency analysis allows for the extraction of short time-frame spectral content where DFT analysis is conducted in sample-limited windows $w[n, m]$, according to (3).

$$V(m, f_n) = \sum_{n=0}^{N-1} v_n w[n-m] e^{\frac{-j2\pi n}{N}} = V(f_n) * w[n] \quad (3)$$

In (3), the windowing function $w[n, m]$ is the analysis window of length m that serves to filter the sampled data. As such, there is a direct trade-off between the size of the window and the bandwidth. The resulting short-time discrete Fourier transform (ST-DFT) can be seen as a convolution of the sampled signal with the window function. Standard window functions include rectangular, Gaussian, Hann, and Hamming [10], though all windows affect the spectral estimates of the signal. Figure 4 illustrates example ST-DFT spectrograms of a single laser-induced transient generated within the CP sub-circuit of the PLL at ~150 MHz operation to illustrate the tradeoffs in time and frequency resolution. The spectrograms in Fig. 4(a)-(c) show the PSD of the PLL's output waveform versus time (seen in Fig. 3) as computed in (3) with a Hamming window function. The spectrograms shown in Fig. 4(d)-(f) were computed from the instantaneous cycle-to-mean phase jitter waveforms determined by (4)

$$\phi_k(v_n) = \frac{2\pi|T_k - E(T_k)|}{E(T_k)} \quad (4)$$

where the signal v_n is sampled at each rising clock edge k, T_k corresponds to the instantaneous period at the k^{th} edge, and $E(T_k)$ is the expected period or population mean [5]. The computation serves to effectively integrate the instantaneous frequency of the output waveform, and thus filters high-frequency noise. The spectrograms shown in Fig. 4(d)-(f) therefore represent unwanted frequency content contained within the closed loop rather than the frequency content in the output waveform. As the nominal bandwidth of the PLL is approximately 5 MHz, the PSD for frequencies less than or equal to 5 MHz can be expected to dominate the spectrogram under normal operation. This can be seen in the spectral content displayed in Fig. 4(f) prior to the SET. This phase

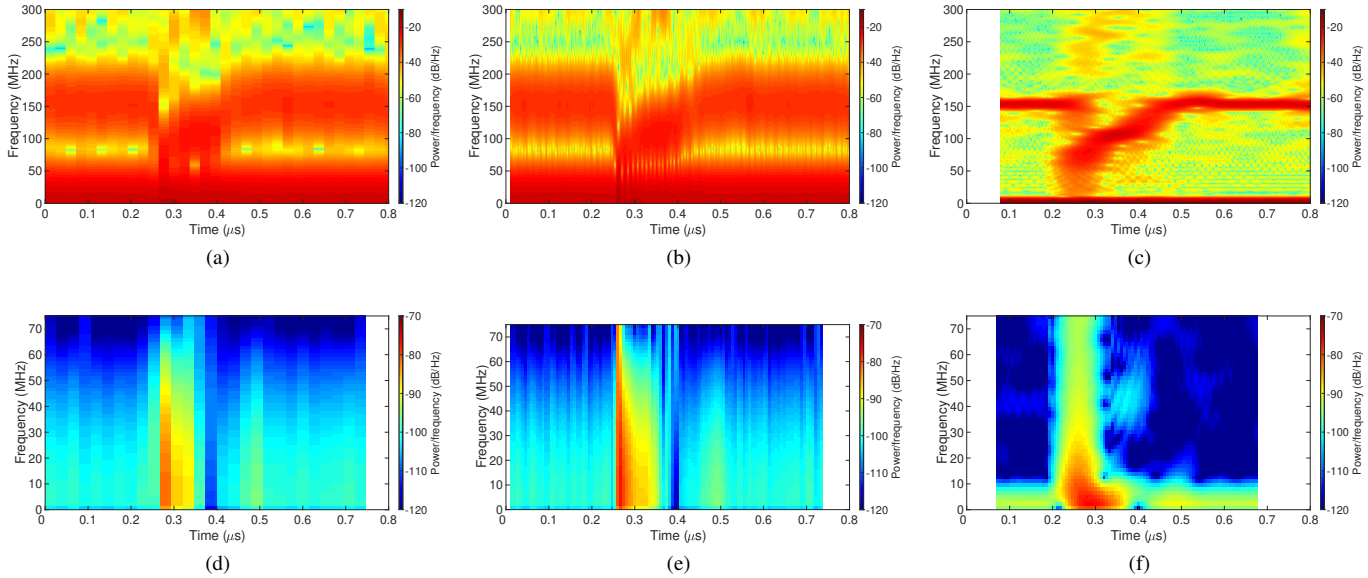

Fig. 4. Spectrograms of a laser-induced transient generated within the CP sub-circuit of the PLL at ∼150 MHz operation to illustrate the tradeoffs in time and frequency resolution. The sample rate of the initial signal was 625 MS/s. The spectrograms in (a)-(c) show the PSD of the PLL's output waveform versus time, whereas the spectrograms in (d)-(f) show the PSD of the cycle-to-mean phase jitter versus time as computed using the ST-DFT with a Hamming window function. Spectrograms (a) and (d) (on left) were computed with a window size of 3% of the total sample length (or 15- and 4-time samples, respectively) and no overlapping windows. Spectrograms (b) and (e) (in middle) were computed with a window size of 3% of the total sample length (or 15- and 4-time samples, respectively) and a window overlap of $n-1$ and $k-1$ samples, respectively. Spectrograms (c) and (f) (on right) were computed with a window size of 20% of the total sample length (or 100- and 22-time samples, respectively) and a window overlap of $n-1$ and $k-1$ samples, respectively.

transformation prior to spectral analysis is particularly useful as it allows for a down-sampling of the output waveform without sacrificing the ability to detect and quantify the erroneous SET.

The spectrograms shown in Fig. 4 are also useful for illustrating the inherent tradeoffs in time and frequency as functions of window size and overlap (which is inversely related to the shift). Spectrograms (a) and (d) (on the left of Fig. 4) were computed with a window size of 3% of the total sample length (or 15- and 4-time samples, respectively) and no overlapping windows (i.e., window shifts of 15- and 4-time samples, respectively). The relatively low number of samples within each window results in an inadequate assessment of the PSD via the ST-DFT methodology. However, overlapping adjacent windows as shown in spectrograms (b) and (e) (in middle of Fig. 4), where window overlaps of $n-1$ and $k-1$ samples were included (i.e. a shift of 1 sample), respectively, improves the assessment of the erroneous spectral content by re-sampling data points within adjacent windows. This can be seen as pin-pointing the erroneous content through a comparison to adjacent content. This is an important point that is critical for the incorporation of statistical measures, as discussed in Section III.B.

While overlapping windows improves the ability to detect an anomaly, the low number of data samples within each window results in significant noise. Spectrograms (c) and (f) (on the right of Fig. 4) were computed with a window size of 20% of the total sample length (or 100- and 22-time samples, respectively) and a window overlap of $n-1$ and $k-1$ samples, respectively. Increasing the window size improves the noise by increasing the number of samples per window. This can be seen as an improved low-pass filter at the sacrifice of time-resolution, as seen in the spectrograms. The transient is clearly visible in both frequency and phase domains with the lowering of the output frequency from the PLL's nominal 150 MHz and the increase in high-frequency content within the loop dynamics; however, there is a smearing of the spectral content in the x-dimension. Nevertheless, the down-sampled spectral phase content shown in Fig. 4(f) amounts to less than 0.19% of the number of spectral samples required to quantify the event shown in Fig. 4(b), corresponding to a decrease of nearly three orders of magnitude (or a 99.8% decrease).

B. Ionizing Radiation Effects Spectroscopy

Ionizing radiation effects spectroscopy (IRES) is a method to augment time-frequency analysis through the statistical measurement of the waveform dynamics. This type of analysis is intended to leverage the computational savings achieved with windowed filtering, as discussed in Section III.A while providing a simple methodology for quantifying and isolating detected events from nominal behavior. IRES is based on Radio Frequency-Distinct Native Attribute (RF-DNA) fingerprinting for the identification of essential statistical features of erroneous signals within a device, circuit, or system. RF-DNA fingerprinting is a waveform-based technique used for augmenting existing wireless network security mechanisms. RF-DNA fingerprinting can be employed in the 1D time or frequency domains or in 2D through time-frequency analysis, as discussed in Section III.A. Works have demonstrated successes in the use of RF-DNA for the identification of unique serial numbers from parts manufactured by the same vendor and containing the same model number [15]–[21].

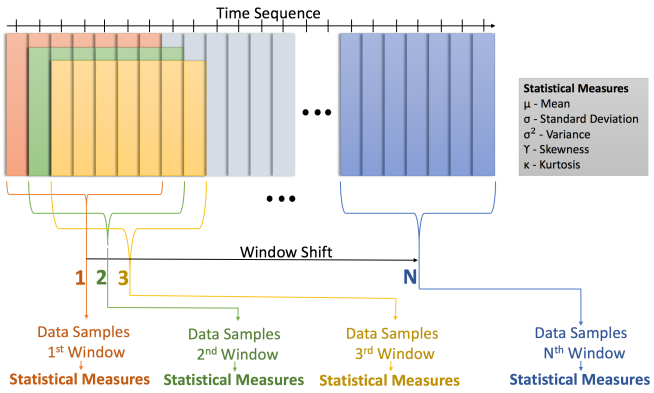

Fig. 5. Illustration of the window sampling method used for the calculation of statistical measures used in IRES.

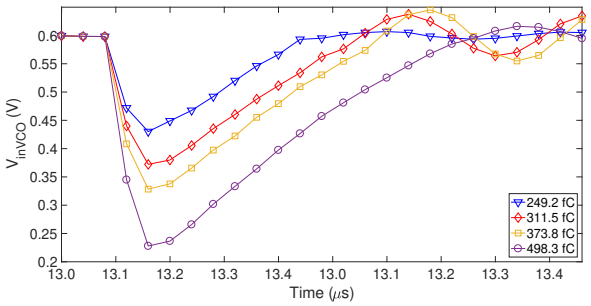

Fig. 6. Simulated ion strikes to NMOS transistors at output of the CP after various levels of charge deposited from a current source. These results show a recovery times between 200 and 300 ns and voltage perturbations between 0.15 and 0.4 V.

Similarly, IRES uses key statistical measures of arbitrary signals within a device, circuit, or system for correlation to radiation vulnerabilities. IRES was first demonstrated in [22] to determine the operational bias voltage and total-ionizing dose (TID) exposure level in RF circuits. IRES images show shifting stochastic behavior with increasing TID levels that are unique for each operational state. These unique states allow for machine-learning models to identify and quantify degradation amidst variation in operational conditions.

In this work, the IRES technique is applied to time-domain signals such that SETs can be identified through statistical measurements of L signal metrics (e.g., cycle-to-mean jitter and instantaneous frequency). Similar to the time-frequency analysis presented in Section III.A, IRES modulates an arbitrary waveform with a window function. Data within the windows are then viewed from a statistical point of view in order to (i) assess the likelihood of SET behavior within a window and (ii) quantify the severity of detected SETs. The use of multi-dimensional statistical analysis allows for easier identification of spurious transients in the presence of noise and allows for ease of integration with statistical models when compared to standard measurement approaches. The technique naturally accounts for variability due to process and measurement uncertainty. IRES images are shown to capture inherent radiation effects mechanisms and the resulting impact on circuit behavior.

Fig. 5 illustrates the window sampling process where descriptive statistics [23] are computed for each window. The statistical measures may include the mean (average of the data values), standard deviation (average distance between an observation and the mean), variance (average of the squared deviations from the mean), skewness (direction and degree of asymmetry), and kurtosis (heaviness of the distribution tails) of an arbitrary signal, for example [23]. In this case, we perform the statistical sampling on the cycle-to-mean jitter feature due to the improved noise performance and low data rate requirement, as discussed in Section III.A. The mean of the instantaneous output frequency is also calculated for each window for a visual of the transient in a traditional form and for comparison to the spectrograms shown in Fig. 4. Once the statistical measures are computed within each window and normalized such that the maximum value of any measure is 1, they are concatenated to form a column vector. These column vectors are arranged as a pseudo-time-sequence, forming an IRES image of the SET characteristic behavior.

IV. Single Event Transient Analysis with IRES

IRES is demonstrated through behavioral simulations of a PLL for the prediction of SET spectrographic data and validated with experimental data captured from TPA laser experiments on PLL circuits designed and fabricated in a 130 nm CMOS technology.

A. Simulation Analysis with IRES

Simulations were performed using a behavioral model to approximate the PLL as a linear system with the ideal design parameters provided in [5]. The PLL model was designed with Verilog-A to match the circuit dynamics of the DUT used for experimental validation. SET simulations were performed with the Cadence Spectre circuit simulator. Reference [5] showed that the SET response of the PLL circuit is dominated by the loop parameters, is largely independent of the ion strike time constants, and is proportional to the deposited charge. Equation (5) shows the expected voltage perturbation (V_e) at the VCO's control voltage versus deposited charge Q_{SET} and the initial transient pulse width t_{SET}.

$$V_e = \frac{Q_{SET} + I_{CP} t_{SET}}{C_{LPF}} \approx \frac{Q_{SET}}{C_{LPF}} \tag{5}$$

In (5), I_{CP} is the CP current, and C_{LPF} is the capacitance of the dominant pole in the LPF. In general, the quantity $I_{CP} t_{SET}$ will be much smaller than Q_{SET} due to the short SET pulse widths in modern CMOS. Thus, a double exponential model for the ion strike was used to create the initial loop perturbation, rather than a more accurate ion strike model. The transient curves for various levels of deposited charge (determined by integrating the ion strike current pulse) are provided in Fig. 6 where the VCO control node (V_{inVCO}) versus time following simulated ion strikes to NMOS transistors at the output of the CP sub-circuit at 260 MHz are provided. Note that this node is internal to the PLL loop and may not be accessible experimentally. Given a linear VCO, V_{inVCO} is proportional to the PLL's output frequency and is an indicator

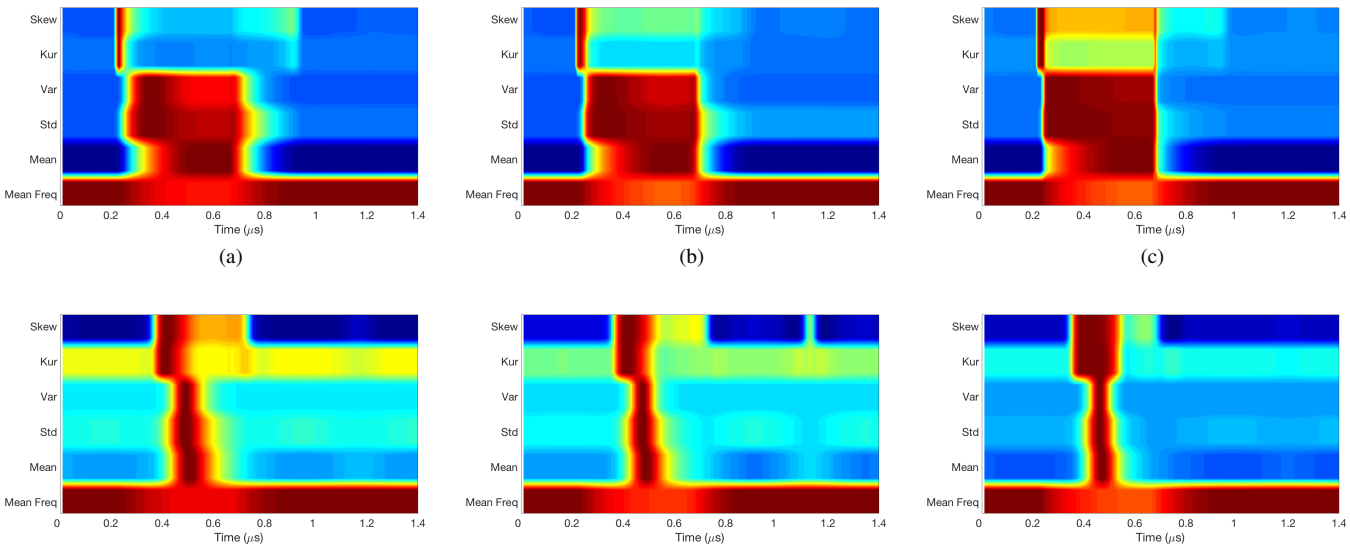

Fig. 7. IRES statistical spectrograms of simulated transients generated at the output of the CP sub-circuit of the PLL at 260 MHz operation. The sample rate of the initial signals shown in Fig. 6 was 10 GS/s. The images in (a)-(c) show the IRES spectrograms of the cycle-to-mean jitter with a rectangular window function (unity). The images in (d)-(f) employ a Gaussian window filter for (a/d) 249.2 fC, (b/e) 373.8 fC, and (c/f) 498.3 fC of deposited charge, respectively. All statistical measures are normalized such that the maximum value is 1.

of the current state of the loop. As expected, the voltage perturbation and recovery time of the PLL increase as the deposited charge increases. These changes in the recovery time and control voltage are gauges of the deposited charge and indicate a representative behavioral model. These simulation results are consistent with other works and indicate adequate loop dynamics for capturing SET phenomena.

The simulated output waveforms of the PLL were sampled at 10 GS/s to generate IRES images of the SET responses for various levels of deposited charge at the output node of the CP sub-circuit. The spectrograms consist of the skewness (Skew), kurtosis (Kur), variance (Var), standard deviation (Std), and mean (Mean) statistical measures of the cycle-to-mean jitter within each sample window of 44 cycles (20% of the cycle-steps). The images also contain the windowed mean of the instantaneous frequency (Mean Freq) for comparison to the ST-DFT spectrograms shown in Fig. 4. The spectrograms in Fig. 7(a)-(c) show the unfiltered IRES spectrograms of the cycle-to-mean jitter. The spectrograms in Fig. 7(d)-(f) employ a Gaussian window filter with $\alpha = 5$ where the standard deviation of the filter of width m is computed according to (6) and the window function given in (7). Finally, the images were generated for deposited charge values of 249.2 fC (left-most images Fig. 7(a) and (d)), 373.3 fC (middle images Fig. 7(b) and (e)), and 498.3 fC (right-most images Fig. 7(c) and (f)).

$$\sigma = \frac{m-1}{2\alpha} \tag{6}$$

$$w[n] = e^{-\frac{1}{2}(\frac{m}{\sigma})^2} \tag{7}$$

As seen in Fig. 7, the statistical measures such as Mean, Std, and Var of the cycle-to-mean jitter are elongated in the x-axis direction for an increased deposited charge. The mean of the instantaneous frequency combined with the statistical measures mentioned previously indicate the longer loop recovery time by the gradual lightening of color. Changes in Skew and Kur of the cycle-to-mean jitter represent abrupt changes in transient behavior. The onset of the SET can be seen as a sudden change in the sample values colored red.

The Var, Std, and Mean of the cycle-to-mean jitter are measures of the charge deposition and collection processes as well as the PLL loop response. For example, the time between the peak Skew and the peak Mean represents the initial charge collection, whereas the magnitude of the Var represents the severity of the event (total energy transferred). The circuit begins to recover following the maximum Mean value, eventually stabilizing where the Mean, Var, and Std return to 0. The overall loop characteristic response can also be seen as the shifts in the mean frequency and the gradual recovery of the loop when the color changes from orange to red, shown on the bottom row of the IRES images. It is important to note that standard measurement techniques generally only capture and quantify the peak and the length of time of the perturbation.

B. Experimental Analysis with IRES

Each waveform from the experimental data consisted of a minimum of 500 timesteps. Cycle-to-mean phase jitter was extracted for each clock cycle in the waveform and used to create a feature vector V. Unless otherwise noted, the experimental data were analyzed with a window consisting of 20% of the total number of cycles and a shift value of 1 (approximately 95% overlap). Gaussian window filters were employed according to (6) and (7) with $\alpha = 5$ identical to those used in the simulations presented in Section IV.A.

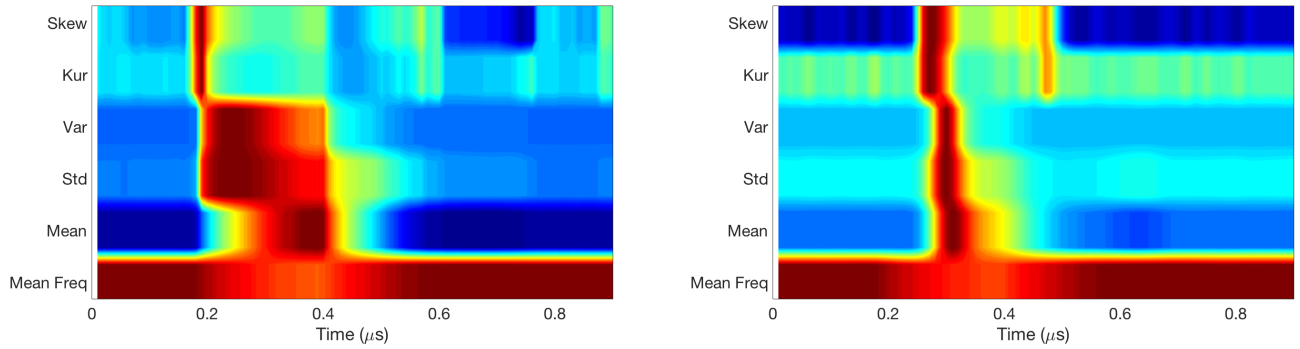

Fig. 8. IRES images of an experimentally measured SET originating from a strike on an NMOS transistor connected to the output node of the CP within the PLL operating at 150 MHz. Six statistical measures were computed within a sliding window sized to 20% of the total sample space and shifted by 1 sample (95% overlap). The spectrograms were computed with (a) rectangular and (b) Gaussian filters. Peaks in Skew and Kur of the cycle-to-mean jitter indicate the start of the SET. The statistical measures of the cycle-to-mean jitter are used to identify radiation and circuit response mechanisms.

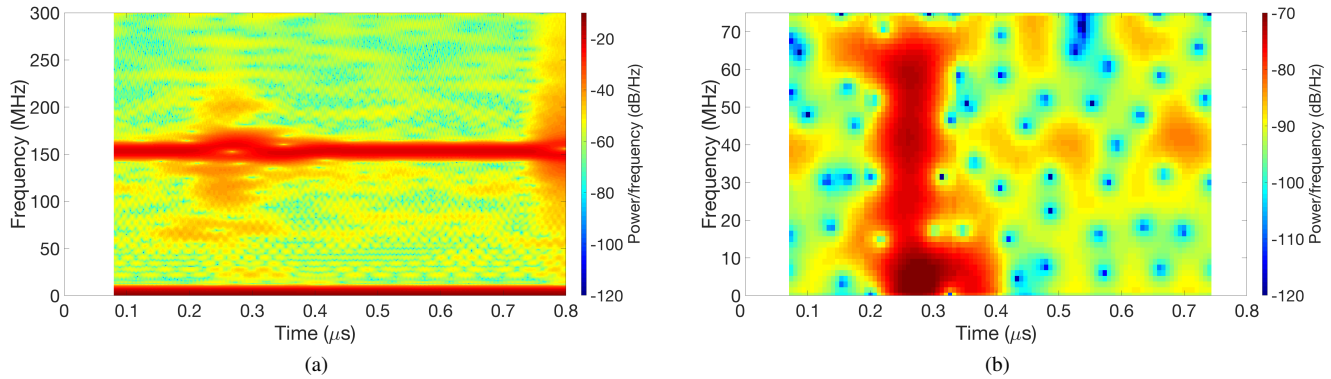

Fig. 9. Spectrograms of a laser-induced transient generated from a strike to a PMOS transistor in the CP sub-circuit of the PLL at 150 MHz operation. The sample rate of the initial signal was 625 MS/s. The spectrograms show (a) the PSD of the PLL's output waveform versus time and (b) the PSD of the cycle-to-mean phase jitter versus time as computed using the ST-DFT with a Hamming window function. Both spectrograms were computed with a window size of 20% of the total sample length (or 100- and 22-time samples, respectively) and a window overlap of $n-1$ and $k-1$ samples, respectively.

Figure 8 shows the (a) unfiltered and (b) filtered IRES images of an experimentally measured SET generated from a laser strike to an NMOS transistor at the output node of the CP within the PLL operating at ∼150 MHz. Skew and Kur of the cycle-to-mean jitter indicate the start of the SET. The statistical measures of the cycle-to-mean jitter are used to identify radiation and circuit response mechanisms. The IRES image indicates that the statistical features are unique to the response signature. Moreover, the experimentally obtained signatures match the predicted images generated from simulations, as seen in Fig. 7. Further, the normalization used to create the IRES images allows for the removal of the magnitude of the ion strike, thus creating a "fingerprint" characteristic of the origins of the ion strike. These characteristic IRES features appear to be inherent to the circuit, the location of the strike, and the charge collection mechanisms.

Previous works have shown that strikes to the PMOS transistors within the CP sub-circuit result in a subtler response when compared to the results shown thus far. Strikes to PMOS transistors in the output switches or current sources inject charge onto the loop capacitor CLPF, thus increasing the instantaneous frequency. According to [5], this positive frequency modulation limits the instantaneous cycle-to-mean phase jitter to a maximum value of 2π radians and is therefore difficult to differentiate from nominal jitter. This effect is illustrated in Fig. 2 where the 2D spatial map of vulnerable nodes within the CP show weaker responses from strikes originating on the PMOS switches and current sources. This effect is further emphasized with the spectrogram of the output waveform computed with ST-DFT analysis in Fig. 9. In Fig. 9, spectrograms of a laser-induced transient generated from a strike to a PMOS transistor in the CP sub-circuit of the PLL at ∼150 MHz operation are shown. The spectrograms show (a) PSD of the PLL's output waveform versus time, and (b) the PSD of the cycle-to-mean phase jitter versus time as computed using the ST-DFT with a Hamming window function. Both spectrograms were computed with a window size of 20% of the total sample length (or 100- and 22-time samples, respectively) and a window overlap of $n-1$ and $k-1$ samples, respectively. These data can be compared to the spectrograms representing a strike to an NMOS transistor in Fig. 3 (c) and (f). While the event is observable, the time boundaries are

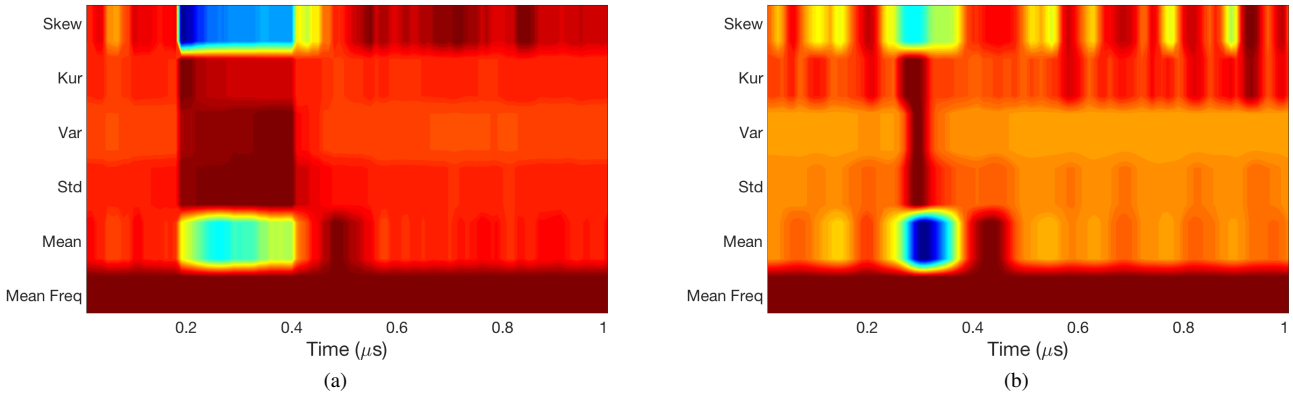

Fig. 10. IRES images of an experimentally measured SET originating from a strike on a PMOS transistor connected to the output node of the CP within the PLL operating at ∼150 MHz. Six statistical measures were computed within a sliding window sized to 20% of the total sample space and shifted by 1 sample (95% overlap). The spectrograms were computed with (a) rectangular and (b) Gaussian filters. Drops in Skew and Kur of the cycle-to-mean jitter indicate the start of the SET. The statistical measures of the cycle-to-mean jitter are used to identify radiation and circuit response mechanisms. The IRES images indicates that the statistical features are unique to the response signature.

difficult to discern due to the required filtering.

The IRES statistical spectrograms shown in Fig. 10, however, can be used to quantify the boundaries of the event, including the onset, peak, and recovery. Figure 10 shows IRES images of the experimentally measured SET shown in Fig. 9. Six statistical measures were computed within a sliding window sized to 20% of the total sample space and shifted by 1 sample (95% overlap). The spectrograms were computed with (a) rectangular and (b) Gaussian filters. Drops in skewness and kurtosis of the cycle-to-mean jitter indicate the start of the SET. These boundaries can then be utilized to perform spectroscopy targeted to the specific temporal location, or to isolate the raw data for further processing, thus alleviating significant computational requirements.

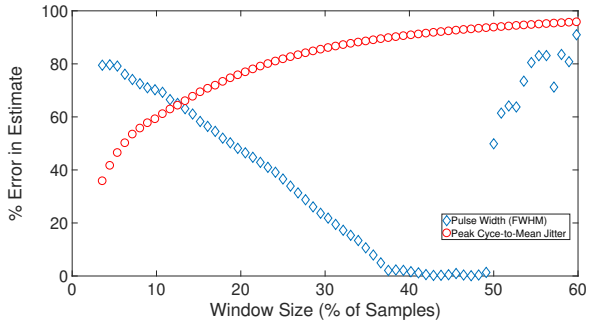

Fig. 11. Percent (%) error in estimates of the magnitude (peak) and pulse-width (full-width half-maximum or FWHM) of the SET extracted from IRES spectrograms versus the window size (in % of total number of samples).

C. Quantification of Error

As the statistical features used in IRES serve as indicators of the SET behavior, the features can be used as an indirect measure of the core transient characteristics, namely the magnitude (peak) and pulse-width of the observable transient. We used the MATLAB software platform to parse the IRES images and extract the local minima and maxima of the statistical measures. These quantities were then used to quantify the peak cycle-to-mean phase jitter (magnitude), and the full-width-half maximum (FWHM) estimate of the SET pulse width. The local maxima of the skewness (or kurtosis) are used to define the total width of the event, whereas the peak in the mean is a direct estimate of the SET magnitude. This analysis can be furthered by examining the difference in the onset of the event (the first peak in skewness) and time at which the peak mean occurs as being the rise-time, whereas the fall-time can be determined as the difference in the time at which the peak mean occurs and the second peak in skewness. Variance and standard deviation measures further serve as indicators of the transient time constants.

This method was evaluated for varying window lengths from approximately 3% of the total sample size to 60% of the total sample size. In each case, the window overlap was $k-1$ samples (corresponding to a shift value of 1). Figure 11 shows the % error in the estimate of the SET magnitude and pulse width versus the window size. The percent error was determined by computing the difference between the parameter as determined from the raw waveform (i.e., the expected value) and that extracted from the IRES spectrograms, divided by the expected value.

As seen in Fig. 11, the % error in the estimate of the pulse width decreases for increasing window size, whereas the % error in the estimate of the magnitude increases with increasing window size. The estimate of the SET pulse width improves with increasing window size as the window size approaches the width of the transient. While the spectral content tends to smear within the window for larger window sizes, the boundaries can be clearly defined with significant window overlap. This has the effect of improving the pulse width estimate while decreasing the ability to estimate the peak accurately. This trend continues for increases in window size until the window is larger than 50% of the total sample size. In this case, the SET boundaries can no longer be delineated. Given the inverse relationship between the two measures, there

exists an optimum window size to balance the error in peak and width measurements.

These results indicate that the IRES technique is useful for the extraction of SET pulses from arbitrarily complex waveforms and allows for estimates of the transient characteristics (e.g., pulse width and amplitude) with a vastly reduced sample size. In this case, SET pulse characteristics were extracted with as little as 0.2% of the data samples. Additionally, the technique enables the detection of subtle changes in characteristics without the need to conduct experimentation under static conditions. These subtle changes are indicators of both the charge collection mechanisms and the resulting circuit responses. IRES not only provides detailed insight into radiation effects mechanisms through a statistical analysis of waveform behavior, but the technique also shows promise in the identification of single-event effects without the need for interrogation of the internal nodes of the circuit. Potential application spaces for IRES include identification of SETs within complex RF waveforms, *in situ* monitoring and analysis of SETs, and automated SET detection assisted by machine learning.

V. Conclusion

This work employs IRES for the characterization of SETs in circuits and systems. The use of multi-dimensional statistical analysis allows for the identification of spurious transients in the presence of noise and for integration with statistical models. This is illustrated through the use of data captured from TPA laser experiments on a PLL designed and fabricated in a 130 nm CMOS technology and further illustrated through the use of behavioral modeling of the circuit dynamics. IRES shows that SETs can be detected through statistical analysis of waveform behavior rather than standard signal measurement, allowing for the capture of the subtle changes in loop recovery time as well as charge dynamics. The technique leverages computational benefits of windowed joint time-frequency analysis, requiring as little as 0.2% of the data samples required in high-resolution DFT analysis, while providing a statistical method for accurately estimating the SET characteristics, such as magnitude and pulse width.

References

[1] S. Buchner and D. McMorrow, "Single-event transients in bipolar linear integrated circuits," *IEEE Transactions on Nuclear Science*, vol. 53, no. 6, pp. 3079–3102, Dec 2006.

[2] T. D. Loveless and W. T. Holman, "Single-event mitigation techniques for analog and mixed-signal circuits," in *Ionizing Radiation Effects in Electronics: From Memories to Imagers*, M. Bagatin and S. Gerardin, Eds. CRC Press, 2016, ch. 9, pp. 229–264.

[3] Y. Boulghassoul, L. W. Massengill, A. L. Sternberg, R. L. Pease, S. Buchner, J. W. Howard, D. McMorrow, M. W. Savage, and C. Poivey, "Circuit modeling of the lm124 operational amplifier for analog single-event transient analysis," *IEEE Transactions on Nuclear Science*, vol. 49, no. 6, pp. 3090–3096, Dec 2002.

[4] T. D. Loveless, L. W. Massengill, W. T. Holman, and B. L. Bhuva, "Modeling and mitigating single-event transients in voltage-controlled oscillators," *IEEE Transactions on Nuclear Science*, vol. 54, no. 6, pp. 2561–2567, Dec 2007.

[5] T. D. Loveless, L. W. Massengill, W. T. Holman, B. L. Bhuva, D. McMorrow, and J. H. Warner, "A generalized linear model for single event transient propagation in phase-locked loops," *IEEE Transactions on Nuclear Science*, vol. 57, no. 5, pp. 2933–2947, Oct 2010.

[6] D. McMorrow, W. T. Lotshaw, J. S. Melinger, S. Buchner, Y. Boulghassoul, L. W. Massengill, and R. L. Pease, "Three-dimensional mapping of single-event effects using two photon absorption," *IEEE Transactions on Nuclear Science*, vol. 50, no. 6, pp. 2199–2207, Dec 2003.

[7] D. McMorrow, W. T. Lotshaw, J. S. Melinger, S. Buchner, and R. L. Pease, "Subbandgap laser-induced single event effects: carrier generation via two-photon absorption," *IEEE Transactions on Nuclear Science*, vol. 49, no. 6, pp. 3002–3008, Dec 2002.

[8] E. W. V. Stryland, H. Vanherzeele, M. A. Woodall, M. J. Soileau, A. L. Smirl, S. Guha, and T. F. Boggess, "Two Photon Absorption, Nonlinear Refraction, And Optical Limiting In Semiconductors," *Optical Engineering*, vol. 24, no. 4, pp. 613 – 623, 1985. [Online]. Available: https://doi.org/10.1117/12.7973538

[9] T. Boggess, K. Bohnert, K. Mansour, S. Moss, I. Boyd, and A. Smirl, "Simultaneous measurement of the two-photon coefficient and free-carrier cross section above the bandgap of crystalline silicon," *IEEE Journal of Quantum Electronics*, vol. 22, no. 2, pp. 360–368, February 1986.

[10] J. Allen, "Short term spectral analysis, synthesis, and modification by discrete fourier transform," *IEEE Transactions on Acoustics, Speech, and Signal Processing*, vol. 25, no. 3, pp. 235–238, June 1977.

[11] T. D. Loveless, B. D. Olson, B. L. Bhuva, W. T. Holman, C. C. Hafer, and L. W. Massengill, "Analysis of single-event transients in integer-*N* frequency dividers and hardness assurance implications for phase-locked loops," *IEEE Transactions on Nuclear Science*, vol. 56, pp. 3489–3498, 2009.

[12] H. H. Chung, W. Chen, B. Bakkaloglu, H. J. Barnaby, B. Vermeire, and S. Kiaei, "Analysis of single events effects on monolithic pll frequency synthesizers," *IEEE Transactions on Nuclear Science*, vol. 53, no. 6, pp. 3539–3543, Dec 2006.

[13] T. Grasser, H. Reisinger, P. . Wagner, F. Schanovsky, W. Goes, and B. Kaczer, "The time dependent defect spectroscopy (tdds) for the characterization of the bias temperature instability," in *2010 IEEE International Reliability Physics Symposium*, May 2010, pp. 16–25.

[14] R. M. Howard, "The power spectral density," in *Principles of Random Signal Analysis and Low Noise Design: The Power Spectral Density and its Applications*. IEEE, 2002, ch. 3.

[15] W. C. Suski, M. A. Temple, M. J. Mendenhall, and R. F. Mills, "Radio frequency fingerprinting commercial communication devices to enhance electronic security," *IJESDF*, vol. 1, pp. 301–322, 2008.

[16] R. W. Klein, M. A. Temple, and M. J. Mendenhall, "Application of wavelet-based rf fingerprinting to enhance wireless network security," *Journal of Communications and Networks*, vol. 11, no. 6, pp. 544–555, Dec 2009.

[17] M. D. Williams, S. A. Munns, M. A. Temple, and M. J. Mendenhall, "Rf-dna fingerprinting for airport wimax communications security," in *2010 Fourth International Conference on Network and System Security*, Sep. 2010, pp. 32–39.

[18] P. K. Harmer, D. R. Reising, and M. A. Temple, "Classifier selection for physical layer security augmentation in cognitive radio networks," in *2013 IEEE International Conference on Communications (ICC)*, June 2013, pp. 2846–2851.

[19] H. J. Patel, M. A. Temple, and R. O. Baldwin, "Improving zigbee device network authentication using ensemble decision tree classifiers with radio frequency distinct native attribute fingerprinting," *IEEE Transactions on Reliability*, vol. 64, no. 1, pp. 221–233, March 2015.

[20] D. R. Reising, M. A. Temple, and J. A. Jackson, "Authorized and rogue device discrimination using dimensionally reduced rf-dna fingerprints," *IEEE Transactions on Information Forensics and Security*, vol. 10, no. 6, pp. 1180–1192, June 2015.

[21] T. J. Bihl, K. W. Bauer, and M. A. Temple, "Feature selection for rf fingerprinting with multiple discriminant analysis and using zigbee device emissions," *IEEE Transactions on Information Forensics and Security*, vol. 11, no. 8, pp. 1862–1874, Aug 2016.

[22] B. Patel, M. Joplin, R. C. Boggs, D. R. Reising, M. W. McCurdy, L. W. Massengill, and T. D. Loveless, "Ionizing radiation effects spectroscopy for analysis of total-ionizing dose degradation in rf circuits," *IEEE Transactions on Nuclear Science*, vol. 66, no. 1, pp. 61–68, Jan 2019.

[23] S. Vergura, G. Acciani, V. Amoruso, G. E. Patrono, and F. Vacca, "Descriptive and inferential statistics for supervising and monitoring the operation of pv plants," *IEEE Transactions on Industrial Electronics*, vol. 56, no. 11, pp. 4456–4464, Nov 2009.